

Dynamic microscopic study of pre-equilibrium giant resonance excitation and fusion in the reactions $^{132}\text{Sn}+^{48}\text{Ca}$ and $^{124}\text{Sn}+^{40}\text{Ca}$

V.E. Oberacker,¹ A.S. Umar,¹ J.A. Maruhn,² and P.-G. Reinhard³

¹*Department of Physics and Astronomy, Vanderbilt University, Nashville, Tennessee 37235, USA*

²*Institut für Theoretische Physik, Goethe-Universität, D-60438 Frankfurt am Main, Germany*

³*Institut für Theoretische Physik, Universität Erlangen, D-91054 Erlangen, Germany*

(Dated: January 26, 2012)

We study pre-equilibrium giant dipole resonance excitation and fusion in the neutron-rich system $^{132}\text{Sn}+^{48}\text{Ca}$ at energies near the Coulomb barrier, and we compare photon yields and total fusion cross sections to those of the stable system $^{124}\text{Sn}+^{40}\text{Ca}$. The dynamic microscopic calculations are carried out on a three-dimensional lattice using both the Time-Dependent Hartree-Fock method and the Density Constrained TDHF method. We demonstrate that the peak of the GDR excitation spectrum occurs at a substantially lower energy than expected for an equilibrated system, thus reflecting the very large prolate elongation of the dinuclear complex during the early stages of fusion. Our theoretical fusion cross-sections for both systems agree reasonably well with recent data measured at HRIBF.

PACS numbers: 21.60.-n, 21.60.Jz

I. INTRODUCTION

Heavy-ion reactions at radioactive ion beam (RIB) facilities enable us to synthesize new exotic neutron-rich nuclei far away from the valley of stability and to study their physical properties. At the HRIBF facility a series of experiments has been carried out with radioactive ^{132}Sn beams on various targets [1–4].

One of the major open questions in fusion reactions of exotic neutron-rich nuclei is the dependence of the fusion cross section (and related observables) on the neutron excess, or equivalently on the total isospin quantum number $T_z = (Z - N)/2$. To reveal possible systematic trends requires both theoretical and experimental studies with a wide variety of projectile and target combinations which are expected to become available at current and future RIB facilities. To be able to pin down the isospin dependence in a fully microscopic theory, it is desirable to choose collision partners which are as simple as possible: projectile and target nuclei should be spherical in their ground state, and the compound nucleus should have a high fission barrier so that the fission component can be ignored (at least at lower beam energies). Ideal reaction partners satisfying these criteria include the neutron-rich system $^{132}\text{Sn}+^{48}\text{Ca}$ and the stable system $^{124}\text{Sn}+^{40}\text{Ca}$ which we investigate in this paper.

If the reaction partners have appreciably different N/Z ratios, the proton and neutron centers of mass of the reacting system may not coincide during the early stages of the collision. In this case, collective oscillations of protons against neutrons on the way to fusion might occur, the so-called pre-equilibrium giant dipole resonance (GDR) [5–9]. In fusion reactions, the shape of the pre-equilibrium di-nuclear complex exhibits a very large prolate deformation as compared to the shape of the equilibrated compound nucleus (see e.g. Ref. [10], Figures 1 and 2). Consequently, the γ -rays emitted during the early phase of fusion contain information about the shape

of the system and provide a cooling effect along the fusion path as well as insight into the charge equilibration.

The time-dependent Hartree-Fock (TDHF) theory provides a useful foundation for a fully microscopic many-body theory of large amplitude collective motion [11, 12] including nuclear molecular resonances, deep-inelastic scattering and heavy-ion fusion, and collective excitations. The earliest TDHF calculations carried out in the 1970's and 1980's were severely limited by computer memory and speed. Hence, these calculations had to make restrictive assumptions such as axial symmetry and the omission of spin-orbit coupling. During the past several years, with a steady increase in computational power, it has become feasible to perform TDHF calculations on a three-dimensional (3D) Cartesian grid with no symmetry restrictions whatsoever and with much more accurate numerical methods [13–16]. At the same time the quality of effective interactions has also been substantially improved [17–21]. Our TDHF code utilizes the full Skyrme interaction, including all of the time-odd terms in the mean-field Hamiltonian [13, 22].

During the past several years, we have developed the density-constrained TDHF method (DC-TDHF) for calculating heavy-ion potentials [23], and we have applied this method to calculate fusion and capture cross sections above and below the barrier. So far, we have studied the systems $^{132}\text{Sn}+^{64}\text{Ni}$ [24], $^{64}\text{Ni}+^{64}\text{Ni}$ [25], $^{16}\text{O}+^{208}\text{Pb}$ [26], $^{132,124}\text{Sn}+^{96}\text{Zr}$ [10], and we have studied the entrance channel dynamics of hot and cold fusion reactions leading to superheavy element $Z = 112$ [27]. In all cases, we have found good agreement between the measured fusion cross sections and the DC-TDHF results. This is rather remarkable given the fact that the only input in DC-TDHF is the Skyrme effective N-N interaction, and there are no adjustable parameters.

This paper is organized as follows: in Section II we summarize the theoretical formalism for pre-equilibrium GDR excitation in heavy-ion fusion reactions with the

TDHF method, and we compare the resulting dipole radiation yields for the neutron-rich system $^{132}\text{Sn}+^{48}\text{Ca}$ to the photon spectra of the stable system $^{124}\text{Sn}+^{40}\text{Ca}$. In Section III, we study total fusion cross sections for both systems. First, we carry out unrestricted TDHF runs at energies above the barrier (no tunneling). Secondly, we calculate the heavy-ion interaction potential $V(R)$ and the coordinate-dependent mass parameter $M(R)$ utilizing the DC-TDHF method. By numerical integration of the Schrödinger equation for the relative coordinate R with the *Incoming Wave Boundary Condition* (IWBC) method, we calculate total fusion cross sections both below and above the barrier, and we compare our theoretical results to recent data measured at HRIBF. Our conclusions are presented in Section IV.

II. TDHF STUDY OF PRE-EQUILIBRIUM GDR EXCITATION

In the present TDHF calculations we use the Skyrme SLy4 interaction [17] for the nucleons including all of the time-odd terms in the mean-field Hamiltonian [13]. The numerical calculations are carried out on a 3D Cartesian lattice. For the two reactions studied here, the lattice spans 50 fm along the collision axis and 30 – 42 fm in the other two directions, depending on the impact parameter. Derivative operators on the lattice are represented by the Basis-Spline collocation method. One of the major advantages of this method is that we may use a relatively large grid spacing of 1.0 fm and nevertheless achieve high numerical accuracy. First we generate very accurate static HF wave functions for the two nuclei on the 3D grid. The static HF equations are solved with the damped gradient iteration method. The initial separation of the two nuclei is 22 fm for central collisions. In the second step, we apply a boost operator to the single-particle wave functions. The time-propagation is carried out using a Taylor series expansion (up to orders 10–12) of the unitary mean-field propagator, with a time step $\Delta t = 0.4$ fm/c.

In TDHF, the dissipation of the relative kinetic energy into internal excitations is due to the collisions of the nucleons with the “walls” of the self-consistent mean-field potential [28, 29]. Because the randomization of the single-particle motion occurs through repeated exchange of nucleons from one nucleus into the other, the equilibration of excitations is rather slow, and it is sensitive to the details of the shape evolution of the composite system. This is in contrast to most classical pictures of nuclear fusion which generally assume near instantaneous, isotropic equilibration.

In Fig. 1 we show the time evolution of isoscalar multipole moments for a head-on collision of Sn on Ca at $E_{\text{cm}} = 130$ MeV. Compared are the two isotopic combinations $^{132}\text{Sn}+^{48}\text{Ca}$ and $^{124}\text{Sn}+^{40}\text{Ca}$. The isoscalar quadrupole moments Q_{20} and the associated quadrupole

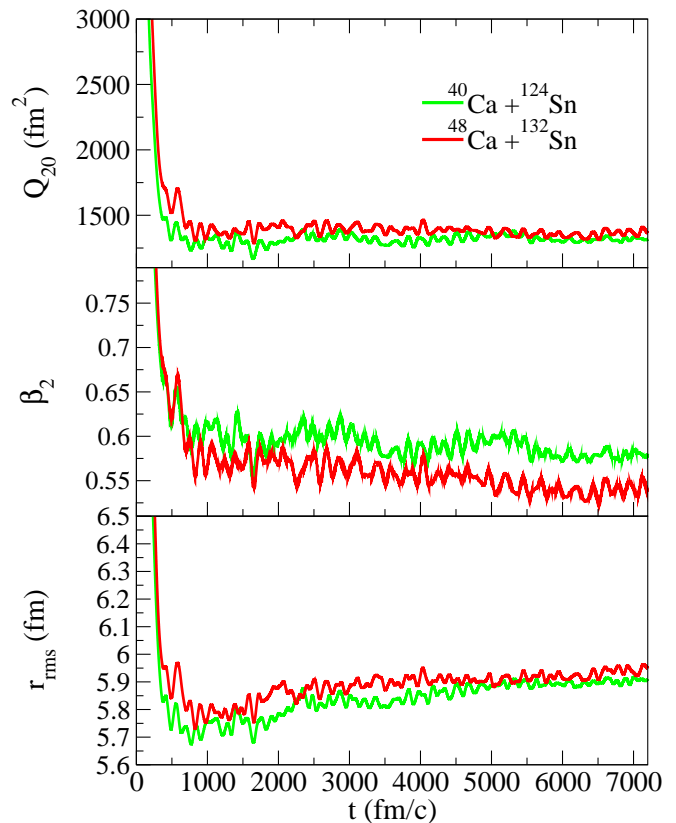


FIG. 1. (Color online) Time evolution of isoscalar multipole moments for a head-on collision of Sn on Ca at $E_{\text{cm}} = 130$ MeV. Two isotopic combinations are considered as indicated.

deformations

$$\beta_{20} = \frac{4\pi}{5} \frac{\langle r^2 Y_{20} \rangle}{A r_{\text{rms}}} \quad (1)$$

show a remarkable stability in the pre-compound state, i.e. after 1000 fm/c. However, this extraordinarily long life-time may be partially due to the frozen occupations (no self-consistent pairing) in the TDHF calculations and partially due to other missing correlations. The center-of-mass coordinate $x_{\text{c.m.}}$ moves less than 0.01 fm. The isoscalar r.m.s. radius shows clearly a small, but steady growth. This is most probably caused by nucleon emission in connection with reflecting boundary conditions. Nucleons which leave the compound system are spread over all box volume and deliver unnaturally larger contributions to the radius. A computation of the radii in an analyzing volume confined to the vicinity of the compound system would probably show the opposite, slightly shrinking radii.

The excitation of the pre-compound giant dipole mode, which is likely when the ions have significantly different N/Z ratio, is a reflection of dynamical equilibration. Dipole excitation results in the emission of γ radiation and possibly pre-equilibrium particle emission which in turn provides an important cooling mechanism

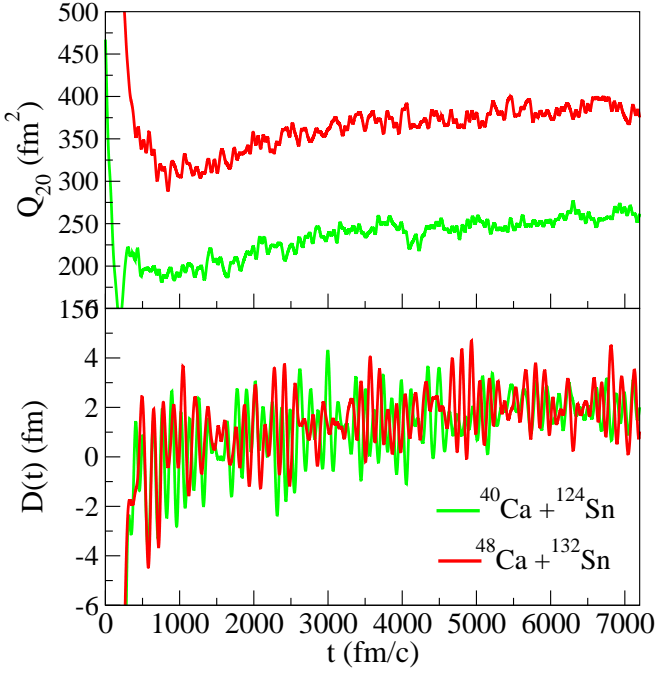


FIG. 2. (Color online) Time evolution of isovector multipole moments for a head-on collision of Sn on Ca at $E_{\text{cm}} = 130$ MeV. Two isotopic combinations are considered as indicated.

during the early stages of the fusion reaction. Several transport simulations like semiclassical Boltzmann-Nordheim-Vlasov [5, 30] as well as microscopic calculations [9, 24, 31, 32] have confirmed this scenario.

To calculate the electric dipole radiation emitted by the time-dependent charge distribution, we consider the dipole operator

$$\mathbf{d} = e \sum_{p=1}^Z \mathbf{r}_p. \quad (2)$$

By adding and subtracting the position vectors of the neutrons we can write this expression in the form

$$\mathbf{d} = \frac{e}{A} \left[N \sum_{p=1}^Z \mathbf{r}_p - Z \sum_{n=1}^N \mathbf{r}_n + Z \left(\sum_{p=1}^Z \mathbf{r}_p + \sum_{n=1}^N \mathbf{r}_n \right) \right]. \quad (3)$$

We now impose the condition that the center-of-mass is fixed at the origin of the coordinate system at all times. As a result, the last term in the round brackets vanishes and we obtain the dipole operator in the form

$$\mathbf{d} = e \frac{NZ}{A} \left[\frac{1}{Z} \sum_{p=1}^Z \mathbf{r}_p - \frac{1}{N} \sum_{n=1}^N \mathbf{r}_n \right]. \quad (4)$$

Let us now consider a central collision in x -direction and

introduce the quantity

$$D(t) = \frac{NZ}{A} \left[\frac{1}{Z} \sum_{p=1}^Z \langle x_p(t) \rangle - \frac{1}{N} \sum_{n=1}^N \langle x_n(t) \rangle \right] \quad (5)$$

which represents the expectation value of the x -component of the dipole operator d_x/e taken with the time-dependent TDHF Slater determinant $|\Phi(t)\rangle$.

In Fig. 2 we show the time evolution of the corresponding isovector quadrupole moment (top panel) and the isovector dipole moment $D(t)$ (bottom panel) for the two systems. It is interesting to compare the isovector dipole moments $D(t)$ for $^{132}\text{Sn} + ^{48}\text{Ca}$ and for $^{124}\text{Sn} + ^{40}\text{Ca}$. The initial amplitude seems to be nearly the same in both cases which may question the argument that the total isospin T_z is responsible for the strong dipole excitations. We have also computed a collision of the symmetric system $^{88}\text{Sr} + ^{88}\text{Sr}$ which ends in a comparable compound state. There is no isovector dipole excitation in this case as expected. There is another interesting feature in that the dipole amplitude remains rather stable for $^{132}\text{Sn} + ^{48}\text{Ca}$ while it shows signs of damping for $^{124}\text{Sn} + ^{40}\text{Ca}$.

Following the bremsstrahlung approach developed by Baran et al. [30] we define the dipole acceleration

$$D''(t) = \frac{d^2 D(t)}{dt^2} \quad (6)$$

and introduce its Fourier transform

$$D''(\omega) = \int_{t_{\min}}^{t_{\max}} D''(t) e^{i\omega t} dt. \quad (7)$$

Alternatively, for nearly harmonic vibrations one can use the expression $|D''(\omega)|^2 = \omega^4 |D(\omega)|^2$, with

$$D(\omega) = \int_{t_{\min}}^{t_{\max}} D(t) e^{i\omega t} \sin^4 \left(\pi \frac{t - t_{\min}}{t_{\max} - t_{\min}} \right) dt. \quad (8)$$

The time filtering \sin^4 is used to smooth out peaks coming from finite integration time. The “power spectrum” of the electric dipole radiation is given by [30]

$$\frac{dP}{dE_\gamma} = \frac{2\alpha}{3\pi E_\gamma} \left| \frac{1}{c} D''(\omega) \right|^2, \quad (9)$$

where $\alpha = e^2/(\hbar c) \approx 1/137$ denotes the fine structure constant.

In Fig. 3 we show results of TDHF calculations of the photon yield given by Eq. 9. For our calculations the use of $D''(t)$ or the alternate expression with $D(t)$ give essentially the same result. Compared are the neutron-rich system $^{132}\text{Sn} + ^{48}\text{Ca}$ and the stable system $^{124}\text{Sn} + ^{40}\text{Ca}$ at the same center-of-mass energy. In performing the full Fourier transform we have cut out the approach phase of the two ions corresponding to times $t < t_{\min} = 800$ fm/c. The upper limit of the time integration is $t_{\max} = 7,200$ fm/c which corresponds to

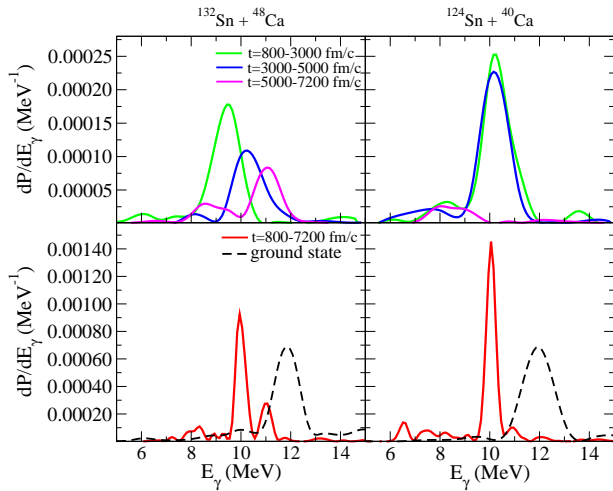


FIG. 3. (Color online) Power spectrum of pre-equilibrium dipole radiation following a central collision at $E_{c.m.} = 130$ MeV of $^{132}\text{Sn}+^{48}\text{Ca}$ (left panel) and $^{124}\text{Sn}+^{40}\text{Ca}$ (right panel). Results are shown for spectral analysis over the whole simulation time (lower panels, red) and over three shorter intervals as indicated (upper panels). The radiation power spectrum of the (deformed) ground state of the compound system is shown by the dashed curve (lower panels).

2.16×10^{-20} s. The lower part (red curve) of the Fig. 3 shows the spectrum obtained for the whole time interval 800 – 7,200 fm/c. We observe that the isovector dipole radiation spectrum shows a peak near 10 MeV for both isotopic combinations. Furthermore, we have also divided the total time span into three intervals and evaluated the power spectra separately for these (see upper panels in Fig. 3). This indicates the time evolution of the power spectra. The case of $^{132}\text{Sn}+^{48}\text{Ca}$ shows a steady upshift of the mean peak and decrease of overall strength. The latter is an obvious effect of damping. The upshift indicates a decreasing system size. This complies with the expectation that the true system radii (evaluated in an analyzing volume) should shrink. The system $^{124}\text{Sn}+^{40}\text{Ca}$ behaves differently. The spectra stay stable during the first two time intervals and shrink dramatically in the third time interval which complies with the fact that the dipole amplitude is visibly smaller at later times (see $D(t)$ panel in Fig. 2). In light of the entrance channel N/Z ratios for the two systems, 1.48 and 1 for $^{124}\text{Sn}+^{40}\text{Ca}$ stable system and 1.64 and 1.4 for the $^{132}\text{Sn}+^{48}\text{Ca}$ neutron-rich system, one can conclude that the system with a larger initial N/Z differential, namely the stable system, should have the stronger initial pre-equilibrium GDR excitation. As can be seen from Fig. 3 this is indeed the case. On the other hand the presence of extra neutrons for the neutron-rich system seem to prolong the life of the GDR suggesting a longer equilibration time for this case.

We have also evaluated the dipole radiation spectra originating from the compound systems in their ground states. Both of these have a quadrupole deformation

$\beta_{20} \approx 0.3$ which is significantly smaller than the deformation of the pre-compound state, $\beta_{20} \approx 0.6$. Figure 3 (lower panels, dashed black curves) shows also the power spectra produced by the compound systems. Because of the smaller deformation the spectra peak at a higher energy, and this peak is well separated from the peak of pre-compound stage.

In order to estimate the energy content in the isovector-dipole oscillations, we have computed the dipole polarizability α_D and find for the pre-compound system $Z/N = 70/110$ the value $\alpha_D = 30 \text{ fm}^3$. The corresponding excitation energy is given by $E_{dip} = e^2 \bar{D}^2 / (2\alpha_D)$. This energy content changes based on what stage of the reaction is considered. During the initial contact phase, where the dipole excitation may be the dominant form of collective excitation the amplitude \bar{D} (see Figure 2) is as large as 5–6 fm, which yields 0.6–0.8 MeV excitation whereas at later stages the dipole amplitude is in the range of 2 – 3 fm resulting in approximately 0.1 – 0.2 MeV excitation. Our calculations of excitation energy based on the DC-TDHF method (see Ref. [33]) for this c.m. energy indicate that the amount of intrinsic excitation energy starts to rise from zero as the two nuclei make contact and reach the value of 40 MeV as the initial composite system is formed. Thus the fraction of the excitation energy carried by the pre-equilibrium GDR can be a large part of the small excitation energy near barrier (by as much as 40% at the barrier peak), while it becomes less than a percent in the interior region.

III. FUSION

A. TDHF calculations at energies above the barrier

Depending upon beam energy and impact parameter, the dominant reaction channels are deep-inelastic and fusion reactions [34]. In general, central collisions and collisions with relatively small impact parameter result in fusion, while larger impact parameters give rise to deep-inelastic reactions. At $E_{c.m.}$ energies above the potential barrier it is possible to carry out standard unrestricted TDHF runs (no tunneling). By varying the impact parameter and plotting the density contours as a function of time, one can easily distinguish between fusion events (one fragment in the exit channel) and deep-inelastic reactions (two fragments).

Let us first consider the case of the neutron-rich system $^{132}\text{Sn}+^{48}\text{Ca}$. The HF initialization run shows that both nuclei are spherical in their ground state, in agreement with HFB calculations and with experimental data. At energy $E_{c.m.} = 130$ MeV we find that impact parameters $< b_{max} = 4.45$ fm result in fusion, while impact parameters $b > 4.45$ fm lead to deep-inelastic reactions. Using the sharp cut-off model, the fusion cross section is given by $\sigma_{fus} = \pi b_{max}^2 = 62.2 \text{ fm}^2 = 622 \text{ mb}$. This result is displayed in Fig. 4. Similar TDHF runs have been carried out at energies $E_{c.m.} = 115, 117, 120, 125$ MeV, and the

corresponding fusion cross sections are also shown in the figure.

When we attempted to calculate fusion cross sections for the stable system $^{124}\text{Sn}+^{40}\text{Ca}$ we found that the HF initialization run correctly predicts a spherical ground state for ^{40}Ca , but ^{124}Sn with non-magic neutron number $N = 74$ shows a prolate quadrupole deformation $\beta_2 = 0.054$ whereas Skyrme-HFB calculations [35, 36] and experiment show this nucleus to be spherical. The unphysical shape is due to the lack of pairing in pure HF. Because the shape of the nucleus is very important for fusion calculations, we have added BCS/Lipkin-Nogami pairing to the HF initialization of ^{124}Sn which results in an approximately spherical shape. During the subsequent TDHF run, we have kept the BCS occupation numbers frozen. This approximation is necessary, because a full 3D-TDHF code with self-consistent pairing for nuclear reactions does not currently exist.

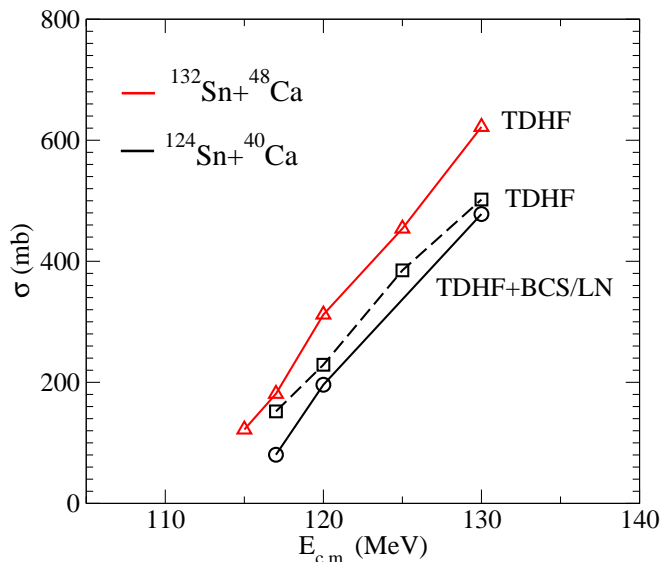


FIG. 4. (Color online) TDHF calculation of the total fusion cross section at energies above the barrier. At fixed $E_{\text{c.m.}}$ energy, the neutron-rich system $^{132}\text{Sn}+^{48}\text{Ca}$ shows a higher cross section than the stable system $^{124}\text{Sn}+^{40}\text{Ca}$.

The resulting total fusion cross sections for $^{124}\text{Sn}+^{40}\text{Ca}$ are also shown in Fig. 4. The solid black line corresponds to TDHF calculations with added pairing (labeled TDHF+BCS/LN), and the dashed line corresponds to pure TDHF which results in a larger fusion cross section for the most favorable orientation of the (unphysical) deformed ^{124}Sn nucleus. We notice that if we plot both systems as a function of the center-of-mass energy, the more massive neutron-rich system shows a larger fusion cross section. Part of this is a trivial size-effect which can be taking out by appropriate scaling factors. We will comment on this issue further when we compare the TDHF cross sections to experimental data (Fig. 9 at the end of Section III).

B. DC-TDHF heavy-ion interaction potential and mass parameter

In the absence of a true quantum many-body theory of barrier tunneling, sub-barrier fusion calculations are reduced to the calculation of a potential barrier between the interacting nuclei and a subsequent calculation of tunneling through the barrier [24]. To date, theoretical studies of fusion cross sections are still dominated by phenomenological methods such as the coupled-channels (CC) approach [37, 38]. In this approach, one either uses empirical ion-ion potentials or one calculates the heavy-ion potential with the double-folding method using measured nuclear densities for projectile and target [39]. In the latter case, one relies on the “frozen density” or “sudden” approximation in which the nuclear densities are unchanged during the computation of the ion-ion potential as a function of the internuclear distance. The frozen density approximation ignores dynamical effects such as neck formation during the nuclear overlap. It has been demonstrated that for deep sub-barrier energies the inner part of the potential barrier plays a very important role [40].

While phenomenological methods provide a useful starting point for the analysis of multitudinous fusion data it is desirable to make contact with the microscopic theories of nuclear structure and reactions. We have developed a fully microscopic method to extract heavy-ion interaction potentials $V(R)$ from the TDHF time-evolution of the dinuclear system. In our DC-TDHF approach [23], the time-evolution takes place with no restrictions. At certain times t during the evolution the instantaneous TDHF density is used to perform a static Hartree-Fock energy minimization. In a typical DC-TDHF run, we utilize a few thousand time steps, and the density constraint is applied every 20 time steps. In this density-constrained method we impose the condition that the total proton and neutron density of the dinuclear system at the ion-ion separation distance $R(t)$ is equal to the instantaneous TDHF density. We refer to the minimized energy as the density constrained energy $E_{\text{DC}}(R(t))$. In the DC-TDHF method the ion-ion interaction potential is given by

$$V(R) = E_{\text{DC}}(R) - E_{A_1} - E_{A_2}, \quad (10)$$

where E_{A_1} and E_{A_2} are the binding energies of the two nuclei obtained with the same effective interaction. For the calculation of the ion-ion separation distance R we use a hybrid method as described in Ref. [26]. At large distances where a visible neck allows us to identify two fragments we compute it as the distance between the centers of mass of the ions. For more compact configurations, we compute R from the mass quadrupole moment Q_{20} as $R = r_0 \sqrt{|Q_{20}|}$ where r_0 is a scale factor to connect the definition smoothly to the large-distance region.

The interaction potentials calculated with the DC-TDHF method incorporate all of the dynamical entrance channel effects such as neck formation, particle exchange,

internal excitations, and deformation effects. While the outer part of the potential barrier is largely determined by the entrance channel properties, the inner part of the potential barrier is strongly sensitive to dynamical effects such as particle transfer and neck formation.

In Fig. 5 we show the heavy-ion interaction potential $V(R)$ for $^{132}\text{Sn}+^{48}\text{Ca}$ calculated with the DC-TDHF method using Eq. (10). The heavy-ion potential depends on the center-of-mass energy and is shown at five different $E_{\text{c.m.}}$ energies. Our results demonstrate that in these heavy systems the potential barrier height increases dramatically with increasing energy $E_{\text{c.m.}}$, and the barrier peak moves inward towards smaller R -values. By contrast, DC-TDHF calculations for light ion systems such as $^{16}\text{O}+^{16}\text{O}$ show almost no energy-dependence even if we increase $E_{\text{c.m.}}$ by a factor of four [33]. Even in reactions between a light and a very heavy nucleus such as $^{16}\text{O}+^{208}\text{Pb}$, we see only a relatively small energy dependence of the barrier height and width [26].

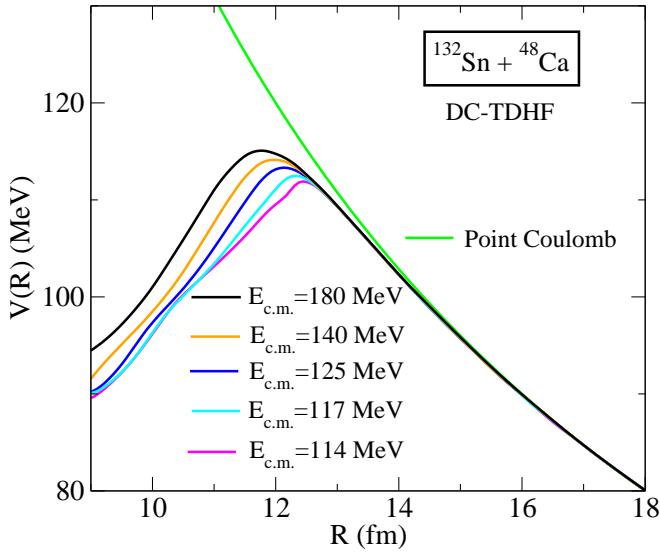


FIG. 5. (Color online) DC-TDHF calculation of the heavy-ion potential $V(R)$ for the neutron-rich system $^{132}\text{Sn}+^{48}\text{Ca}$. The energy-dependent potential is shown at five $E_{\text{c.m.}}$ energies. The point Coulomb potential is given for comparison.

In addition to the ion-ion potential, it is also possible to compute the corresponding coordinate dependent mass parameter $M(R)$ using energy conservation at zero impact parameter

$$M(R) = \frac{2[E_{\text{c.m.}} - V(R)]}{\dot{R}^2}, \quad (11)$$

where the collective velocity \dot{R} is directly obtained from the TDHF evolution and the potential $V(R)$ from the density constraint calculations.

In Fig. 6 we show the mass parameter $M(R)$ calculated from Eq. (11) at four different energies $E_{\text{c.m.}}$. As expected, at large distance R the mass $M(R)$ is equal to the reduced mass μ of the system. At smaller distances,

when the nuclei overlap, the mass parameter increases in all cases. Like the heavy-ion potential, the mass parameter shows a strong dependence on energy: at higher energies, $M(R)$ rises smoothly with decreasing R . However, for the lowest energies which are only a few MeV above the corresponding potential barrier, the mass parameter shows a pronounced peak. This is due to the fact that the velocity \dot{R} in the denominator of Eq. (11) becomes small as the ions approach each other, reaches its minimum at the top of the barrier, and then increases again at smaller R -values.

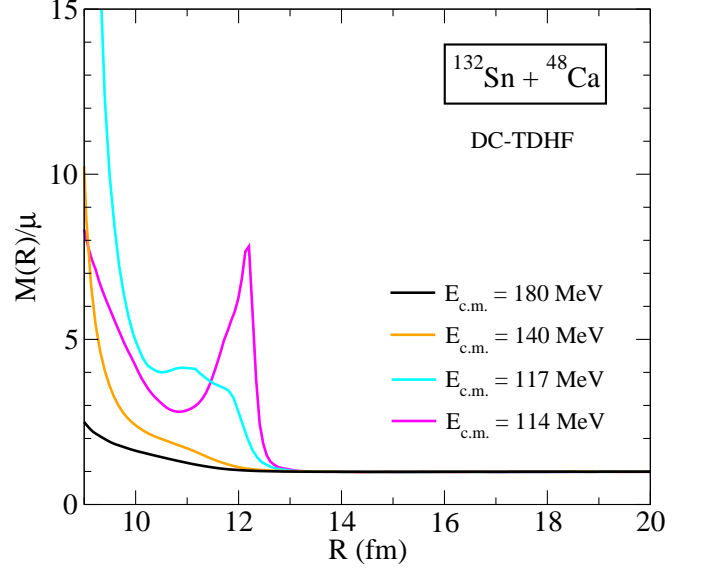


FIG. 6. (Color online) Microscopic mass parameter $M(R)$ (in units of the reduced mass μ), calculated at several $E_{\text{c.m.}}$ energies.

The total fusion cross section is given by

$$\sigma_{\text{fus}}(E_{\text{c.m.}}) = \frac{\pi \hbar^2}{2\mu E_{\text{c.m.}}} \sum_{\ell=0}^{\infty} (2\ell+1) T_{\ell}(E_{\text{c.m.}}). \quad (12)$$

The potential barrier penetrabilities T_{ℓ} are obtained from the numerical solution of the Schrödinger equation for the relative coordinate R . Instead of solving the Schrödinger equation with coordinate dependent mass parameter $M(R)$ for the heavy-ion potential $V(R)$, it is numerically advantageous to use the constant reduced mass μ and to transfer the coordinate-dependence of the mass to a scaled potential $U(\bar{R})$ using the scale transformation

$$d\bar{R} = \left(\frac{M(R)}{\mu} \right)^{\frac{1}{2}} dR. \quad (13)$$

Integration of Eq. (13) yields

$$\bar{R} = f(R) \iff R = f^{-1}(\bar{R}). \quad (14)$$

As a result of this point transformation, the scaled heavy-ion potential is given by the expression

$$V(R) = V(f^{-1}(\bar{R})) = U(\bar{R}). \quad (15)$$

In Fig. 7 we compare the original heavy-ion potential $V(R)$ (solid lines) corresponding to the mass parameter $M(R)$ to the transformed potential $U(\bar{R})$ (dashed lines) calculated from Eq. (15) which corresponds to the constant reduced mass μ . We observe that the coordinate-dependent mass changes only the interior region of the potential barriers, and this change is most pronounced at low $E_{c.m.}$ energies.

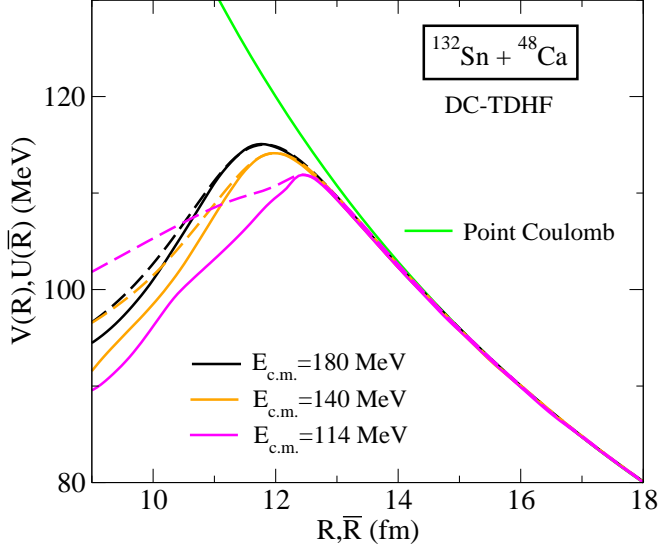


FIG. 7. (Color online) Solid lines: original heavy-ion potentials $V(R)$ corresponding to the mass parameter $M(R)$. Dashed lines: transformed potentials $U(\bar{R})$ corresponding to the reduced mass μ .

The Schrödinger equation corresponding to the constant reduced mass μ and the scaled potential $U(\bar{R})$ has the familiar form

$$\left[\frac{-\hbar^2}{2\mu} \frac{d^2}{d\bar{R}^2} + \frac{\hbar^2 \ell(\ell+1)}{2\mu \bar{R}^2} + U(\bar{R}) - E_{c.m.} \right] \psi_\ell(\bar{R}) = 0. \quad (16)$$

By numerical integration of Eq. (16) using the well-established *Incoming Wave Boundary Condition* (IWBC) method [41, 42] we obtain the barrier penetrabilities T_ℓ which determine the total fusion cross section (12).

C. Fusion cross sections for $^{132}\text{Sn} + ^{48}\text{Ca}$ and for $^{124}\text{Sn} + ^{40}\text{Ca}$

In Fig. 8 we show the total fusion cross section for the neutron-rich system $^{132}\text{Sn} + ^{48}\text{Ca}$. The cross sections obtained with unrestricted TDHF runs above the barrier (see Fig. 4) are indicated by squares. In addition, we display results obtained with the DC-TDHF method which can be used at energies $E_{c.m.}$ below and above the potential barriers. The dashed lines correspond to calculations using the transformed potential $U(\bar{R})$ in Fig. 7 at three different energies. We observe that at high energies, $E_{c.m.} = 135 - 140$ MeV, all of the energy-dependent

heavy-ion potentials yield the same fusion cross section. However, these three potentials yield substantially different cross sections at $E_{c.m.}$ energies near and below the barrier. In particular, we observe that the heavy-ion potential calculated at the lowest possible energy $E_{c.m.} = 114$ MeV (with a barrier height of 111.9 MeV) gives by far the largest fusion cross section at sub-barrier energies. According to theory, at a given $E_{c.m.}$ energy, one should use the heavy-ion potential calculated at this energy. We call this the “ $E_{c.m.}$ -specific potential”. The corresponding total fusion cross sections are given by the solid black line in Fig. 8, and we can see that these DC-TDHF results are in perfect agreement with the unrestricted TDHF runs at above-barrier energies.

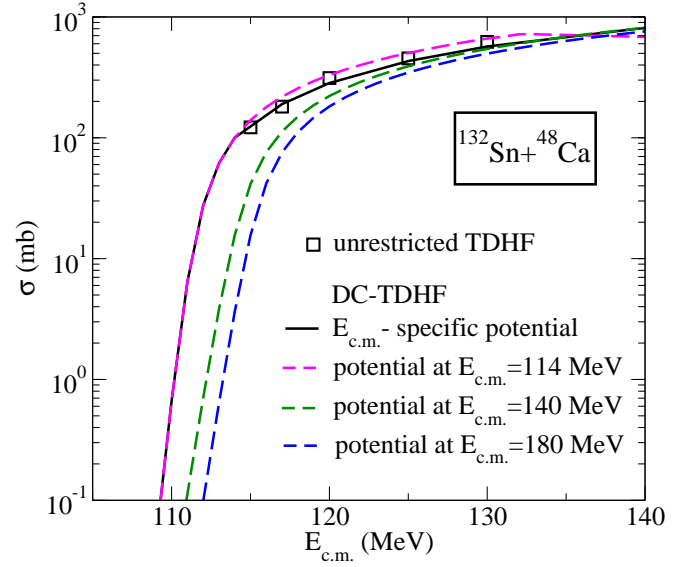


FIG. 8. (Color online) Total fusion cross section for the neutron-rich system $^{132}\text{Sn} + ^{48}\text{Ca}$. Compared are DC-TDHF calculations using the energy-dependent heavy-ion potential in Fig. 7 with unrestricted TDHF calculations (see Fig. 4) at energies above the barrier.

In Fig. 9 we compare our theoretical fusion cross sections for $^{132}\text{Sn} + ^{48}\text{Ca}$ and $^{124}\text{Sn} + ^{40}\text{Ca}$ to experimental data obtained at HRIBF [3, 4]. The data for the latter system agree with earlier measurements by Scarlascara *et al.* [43]. In order to take out trivial size-effects, the HRIBF experimentalists decided to scale their measured fusion cross sections and center-of-mass energies as follows [3]: Defining the size parameter for the composite system

$$R_0 = A_1^{1/3} + A_2^{1/3} \quad (17)$$

the fusion cross section is scaled according to

$$\sigma \rightarrow \sigma/R_0^2 \quad (18)$$

Using the definition of the Coulomb barrier height parameter

$$B_0 = Z_1 Z_2 / R_0 \quad (19)$$

the center-of-mass energy is scaled as follows

$$E_{c.m.} \rightarrow E_{c.m.}/B_0 \quad (20)$$

This scaling procedure yields the same total fusion cross section at high energies for all measured Sn+Ca isotopes. Note that when one corrects for nuclear size effects, the scaled fusion cross sections for the neutron-rich system $^{132}\text{Sn}+^{48}\text{Ca}$ are *lower* than the fusion cross sections for the stable $^{124}\text{Sn}+^{40}\text{Ca}$ system, in contrast to the absolute cross sections plotted in Fig. 4. In the case of $^{124}\text{Sn}+^{40}\text{Ca}$, we are only able to compare the experimental data to our unrestricted TDHF runs at above-barrier energies (see Fig. 4). As we pointed out in Section III.A, these runs were initialized with BCS/Lipkin-Nogami pairing for ^{124}Sn , with the BCS occupation numbers kept frozen during the collision. Unfortunately, this approximation cannot be utilized in the DC-TDHF method because the static HF solution coupled with a constraint on the instantaneous TDHF density for the combined system requires the reevaluation of the occupation numbers for the lowest energy solution. The good agreement between the measured fusion cross sections and our theoretical results is quite remarkable because the only input in TDHF and DC-TDHF is the Skyrme N-N interaction with no adjustable parameters.

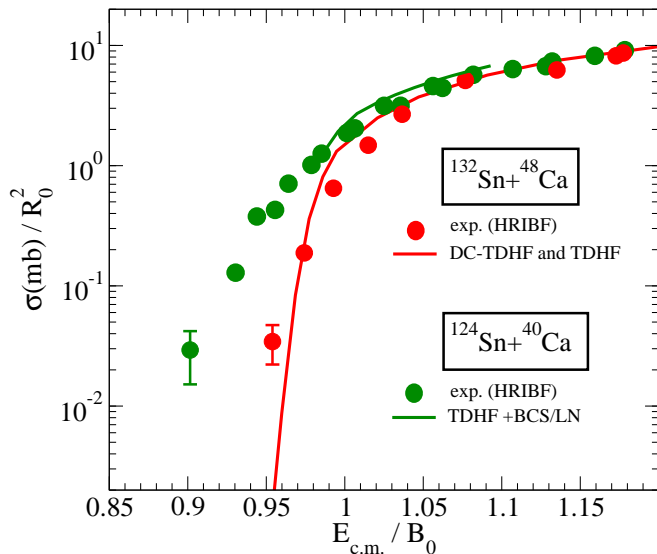


FIG. 9. (Color online) Comparison between scaled experimental fusion cross sections [3] and theoretical results obtained with the DC-TDHF method and with unrestricted TDHF.

IV. SUMMARY

In this paper, we present dynamic microscopic calculations of pre-equilibrium giant dipole resonance excitation and fusion in the neutron-rich system $^{132}\text{Sn}+^{48}\text{Ca}$ at energies near the Coulomb barrier, and we compare photon yields and total fusion cross sections to those of the stable system $^{124}\text{Sn}+^{40}\text{Ca}$. The numerical calculations are carried out on a 3D lattice using both the Time-Dependent Hartree-Fock (TDHF) method and the recently developed Density Constrained TDHF method (DC-TDHF).

Regarding pre-equilibrium GDR excitation, we demonstrate that the peak of the dipole radiation spectrum occurs at a substantially lower energy than expected for an equilibrated system, thus reflecting the very large prolate elongation of the di-nuclear complex during the early stages of fusion.

In addition, we study total fusion cross sections for both systems. First, we carry out unrestricted TDHF runs at energies above the barrier (no tunneling). Secondly, we calculate the heavy-ion interaction potential $V(R)$ and the coordinate-dependent mass parameter $M(R)$ utilizing the DC-TDHF method. Our results demonstrate that in these heavy systems the potential barrier height increases dramatically with increasing energy $E_{c.m.}$, and the barrier peak moves inward towards smaller R -values, in contrast to light ion systems such as $^{16}\text{O}+^{16}\text{O}$ which show almost no energy-dependence.

By numerical integration of the Schrödinger equation for the relative coordinate R with the *Incoming Wave Boundary Condition* (IWBC) method, we calculate total fusion cross sections both below and above the barrier. We emphasize that the only input in our microscopic calculations is the Skyrme N-N interaction, with no adjustable parameters whatsoever. We find that our theoretical fusion cross sections for both systems agree reasonably well with recent data measured at HRIBF.

ACKNOWLEDGMENTS

This work has been supported by the U.S. Department of Energy under Grant No. DE-FG02-96ER40963 with Vanderbilt University, and by the German BMBF under Contracts No. 06ER9063 and No. 06FY9086.

-
- [1] J. F. Liang *et al.*, Phys. Rev. Lett. **91**, 152701 (2003); **96**, 029903(E) (2006).
 - [2] J. F. Liang, D. Shapira, C. J. Gross, R. L. Varner, J. R. Beene, P. E. Mueller, and D. W. Stracener, Phys. Rev. C **78**, 047601 (2008).
 - [3] J.F. Liang, EPJ Web of Conferences **17**, 02002 (2011).
 - [4] J.J. Kolata, A. Roberts, A. Howard, D. Shapira, J.F. Liang, C.J. Gross, R.L. Varner, Z. Kohley, A. Villano, H. Amro, W. Loveland and E. Chavez, "Fusion of $^{124,132}\text{Sn}+^{40,48}\text{Ca}$ ", to be submitted to PRC.
 - [5] P. Chomaz, M. Di Toro, and A. Smerzi, Nucl. Phys. A **563**, 509 (1993).

- [6] S. Flibotte, et. al. Phys. Rev. Lett. **77**, 1448 (1996).
- [7] V. Baran, D. M. Brink, M. Colonna, and M. Di Toro, Phys. Rev. Lett. **87**, 182501 (2001).
- [8] C. Simenel, Ph. Chomaz, and G. de France, Phys. Rev. Lett. **86**, 2971 (2001).
- [9] A. S. Umar, M. R. Strayer, R. Y. Cusson, P. -G. Reinhard, and D. A. Bromley, Phys. Rev. C **32**, 172 (1985).
- [10] V. E. Oberacker, A. S. Umar, J. A. Maruhn, and P.-G. Reinhard, Phys. Rev. C **82**, 034603 (2010).
- [11] J. W. Negele, Rev. Mod. Phys. **54**, 913 (1982).
- [12] R. Y. Cusson, P.-G. Reinhard, M. R. Strayer, J. A. Maruhn, and W. Greiner, Z. Phys. A **320**, 475 (1985).
- [13] A. S. Umar and V. E. Oberacker, Phys. Rev. C **73**, 054607 (2006).
- [14] Lu Guo, J. A. Maruhn, P.-G. Reinhard, and Y. Hashimoto, Phys. Rev. C **77**, 041301(R) (2008).
- [15] Kouhei Washiyama and Denis Lacroix, Phys. Rev. C **78**, 024610 (2008).
- [16] David J. Kedziora and Cédric Simenel, Phys. Rev. C **81**, 044613 (2010).
- [17] E. Chabanat, P. Bonche, P. Haensel, J. Meyer and R. Schaeffer, Nucl. Phys. **A635**, 231 (1998); **A643**, 441(E) (1998).
- [18] M. Bender, P.-H. Heenen, and P.-G. Reinhard, Rev. Mod. Phys. **75**, 121 (2003).
- [19] P. Klüpfel, P.-G. Reinhard, T. J. Bürvenich, and J. A. Maruhn, Phys. Rev. C **79**, 034310 (2009).
- [20] S. Goriely, S. Hilaire, A. J. Koning, M. Sin, and R. Capote, Phys. Rev. C **79**, 024612 (2009).
- [21] M. Kortelainen, T. Lesinski, J. Moré, W. Nazarewicz, J. Sarich, N. Schunck, M. V. Stoitsov, and S. Wild, Phys. Rev. C **82**, 024313 (2010).
- [22] Y. M. Engel, D. M. Brink, K. Goeke, S. J. Krieger, and D. Vautherin, Nucl. Phys. A **249**, 215 (1975).
- [23] A. S. Umar and V. E. Oberacker, Phys. Rev. C **74**, 021601(R) (2006).
- [24] A. S. Umar and V. E. Oberacker, Phys. Rev. C **76**, 014614 (2007).
- [25] A. S. Umar and V. E. Oberacker, Phys. Rev. C **77**, 064605 (2008).
- [26] A. S. Umar and V. E. Oberacker, Eur. Phys. J. A **39**, 243 (2009).
- [27] A. S. Umar, V. E. Oberacker, J. A. Maruhn, and P.-G. Reinhard, Phys. Rev. C **81**, 064607 (2010).
- [28] D. H. E. Gross, Nucl. Phys. A **240**, 472 (1975).
- [29] J. Blocki, Y. Boneh, J. R. Nix, J. Randrup, M. Robel, A. J. Sierk, and W. J. Swiatecki, Ann. Phys. **113**, 330 (1978).
- [30] V. Baran et al., Nucl. Phys. A **600**, 111 (1996).
- [31] C. Simenel, Ph. Chomaz, and G. de France, Phys. Rev. C **76**, 024609 (2007).
- [32] V. Baran, C. Rizzo, M. Colonna, M. Di Toro, and D. Pierroutsakou, Phys. Rev. C **79**, 021603(R) (2009).
- [33] A. S. Umar, V. E. Oberacker, J. A. Maruhn, and P.-G. Reinhard, Phys. Rev. C **80**, 041601(R) (2009).
- [34] P. Armbruster, Ann. Rev. Nucl. Part. Sci. **35**, 135 (1985).
- [35] J. Dobaczewski, M.V. Stoitsov, W. Nazarewicz, *Skyrme-HFB deformed nuclear mass table*, AIP Conference Proceedings Volume 726, ed. R. Bijker, R.F. Casten, A. Frank (American Institute of Physics, New York, 2004) p. 51, nucl-th/0404077.
- [36] A. Blazkiewicz, V.E. Oberacker, A.S. Umar, and M. Stoitsov, Phys. Rev. C **71**, 054321 (2005).
- [37] H. Esbensen, C. L. Jiang, and A. M. Stefanini, Phys. Rev. C **82**, 054621 (2010).
- [38] Takatoshi Ichikawa, Kouichi Hagino, and Akira Iwamoto, Phys. Rev. Lett. **103**, 202701 (2009).
- [39] G.R. Satchler and W. G. Love, Phys. Rep. **55**, 183 (1979).
- [40] Takatoshi Ichikawa, Kouichi Hagino, and Akira Iwamoto, Phys. Rev. C **75**, 057603 (2007).
- [41] K. Hagino and Y. Watanabe, Phys. Rev. C **76**, 021601(R) (2007).
- [42] G. H. Rawitscher, Phys. Rev. **135**, 605 (1964).
- [43] F. Scarlassara, S. Beghini, G. Montagnoli, G.F. Segato, D. Ackermann, L. Corradi, C.J. Lin, A.M. Stefanini, and L.F. Zheng, Nucl. Phys. **A672**, 99 (2000).